

# Heavy Neutrinos across the Electroweak-to-Multi-TeV Frontier via Novel ML-Enhanced Probes

Yin-Fa Shen<sup>a,1</sup>, Alfredo Gurrola<sup>b,1</sup>, Francesco Romeo<sup>c,1</sup>, Denis Rathjens<sup>d,1</sup>,  
Andres Flórez<sup>e,2</sup>

<sup>1</sup>Department of Physics and Astronomy, Vanderbilt University, Nashville, TN, 37235, USA.

<sup>2</sup>Department of Physics, Universidad de los Andes, Bogotá, Colombia.

Received: / Accepted:

**Abstract** We propose a new strategy to probe heavy neutrinos with non-universal fermion couplings at the Large Hadron Collider (LHC) using a novel production mechanism and machine-learning algorithms. Focusing on proton–proton collisions at  $\sqrt{s} = 13.6$  TeV, we investigate final states containing a charged lepton, missing transverse energy, and two jets. For heavy neutrino masses below  $\mathcal{O}(1)$  TeV, production is dominated by the  $s$  channel process. At higher masses, vector boson fusion becomes the dominant production mechanism, with cross sections that decrease slowly as the heavy neutrino mass increases. We simulate both signal and Standard Model background events and employ gradient-boosted decision trees to optimize event classification. Assuming an integrated luminosity of  $3000 \text{ fb}^{-1}$ , expected for the high-luminosity, and considering realistic statistical and systematic uncertainties, we find that heavy neutrinos in the mass range  $50 \text{ GeV}–10 \text{ TeV}$  can be probed with sensitivity to the mixing parameter  $|V_{\ell N}|^2$  spanning from  $\mathcal{O}(10^{-5})$  to 1. This approach enhances the discovery potential for heavy neutrinos and provides a complementary pathway to existing search strategies.

## 1 Introduction

Searching for new physics beyond the Standard Model (SM) remains a central goal in particle physics. Compelling evidence for physics beyond the minimal SM already exists in the neutrino sector—namely, neutrino

<sup>a</sup>e-mail: yin-fa.shen@Vanderbilt.Edu

<sup>b</sup>e-mail: alfredo.gurrola@Vanderbilt.Edu

<sup>c</sup>e-mail: francesco.romeo@cern.ch

<sup>d</sup>e-mail: denis.rathjens@cern.ch

<sup>e</sup>e-mail: ca.florez@uniandes.edu.co

oscillations [1–3], which imply nonzero but tiny neutrino masses [4]. While such masses could, in principle, arise from Yukawa couplings analogous to those in the quark sector, the required couplings would need to be unnaturally small [4]. To address this issue, various theoretical frameworks have been proposed to naturally explain the smallness of neutrino masses [5–14]. A common feature among many of these models is the presence of heavy Majorana neutrinos, which generate light neutrino masses inversely proportional to a large mass scale through the seesaw mechanism [5–7]. A key phenomenological prediction of this mechanism is the existence of heavy neutrinos. Therefore, searching for such heavy states is essential for testing the seesaw mechanism and potentially uncovering the origin of neutrino masses.

In seesaw-inspired models, the masses of heavy neutrinos can span a vast range, from the eV scale up to  $10^{16}$  GeV [15]. For heavy neutrinos lighter than  $\mathcal{O}(1)$  GeV, constraints arise from meson decays [16–22] and neutrinoless double-beta decay ( $0\nu\beta\beta$ ) [23]. At higher masses, electroweak precision data (EWPD) provide useful limits [24, 25], while extensive direct searches have been carried out at LEP and the LHC by experiments such as ALEPH, DELPHI, CMS, and ATLAS [26–40].

For masses up to  $\mathcal{O}(10^2)$  GeV, considerable effort has been devoted to assessing the discovery prospects at future lepton colliders such as CEPC and FCC-ee [41–51]. At even higher masses, the LHC remains the primary facility for probing heavy neutrinos: in the sub-TeV region, they can be resonantly produced and their decay products fully reconstructed, whereas at larger masses the production cross section becomes increasingly suppressed by phase space [52, 53]. In this regime,  $t$  channel mechanisms such as vector boson fusion (VBF) offer a more robust alternative, as their cross section de-

grades more slowly with the heavy neutrino mass [54–57]. As a result, an inclusive simulation and search strategy for the process  $pp \rightarrow \mu\nu jj$ , which receives contributions from both resonant and  $t$  channel diagrams, ensures coverage over a wide range of heavy neutrino masses.

In this work, we analyze and study simulated signal and background samples to develop a new novel strategy to probe heavy neutrinos in proton–proton ( $pp$ ) collisions at the LHC with a center-of-mass energy of  $\sqrt{s} = 13.6$  TeV. We focus on the final state  $\ell\nu jj$ , where  $\ell$  and  $\nu$  denote a charged lepton and a (light) neutrino, respectively, and  $jj$  denotes two jets. Representative Feynman diagrams contributing to signal processes are shown in Fig. 1. Owing to the nature of the Majorana neutrino, lepton number conservation does not constrain the flavor of the light neutrino. Since the light neutrino escapes detection and contributes only to missing transverse energy, summing over its flavor is experimentally motivated. This also enables the exploration of potential lepton-universality violations in these scenarios.

To improve sensitivity, we employ gradient-boosted decision trees (BDTs) [58], trained and tested on kinematic observables of simulated events. Using the BDT output, we compute the signal significance and derive the corresponding sensitivity to the heavy–light neutrino mixing parameters, assuming an integrated luminosity of  $3000 \text{ fb}^{-1}$  expected for the high-luminosity LHC (HL-LHC). Our results indicate that for heavy neutrino masses in the range 50–10000 GeV, the expected sensitivity to the mixing parameter extends from  $\mathcal{O}(10^{-5})$  to  $\mathcal{O}(1)$ , representing an improvement over current experimental limits.

The remainder of this paper is organized as follows. In Section 2, we briefly review the seesaw mechanism and define the relevant model parameters. In Section 3, we describe the generation of signal samples for various heavy neutrino masses, together with the background samples, and present the associated cross sections. In Section 4, we explain the application of BDTs to event classification and discuss the resulting performance. In Section 5, we present the expected sensitivity contours and uncertainty bands for the mixing parameters derived from the BDT analysis under different scenarios. Finally, we conclude by emphasizing that this strategy provides a promising and complementary approach for probing heavy neutrinos in the mass range 50–10000 GeV.

## 2 Theoretical Setup

Following the spirit of the seesaw mechanism [5–7] and the principle of gauge invariance, the simplest renormalizable Lagrangian terms involving neutrino masses are:

$$\mathcal{L}_\nu \ni \frac{1}{2}i\bar{R}_i\partial R_i - y_{ij}\bar{R}_i\tilde{\Phi}^\dagger L_j - \frac{1}{2}(M_N)_{ij}\bar{R}_iR_j^C + \text{h.c.}, \quad (1)$$

where the first term represents the kinetic term for the right-handed Majorana neutrino field,  $\tilde{\Phi}$  is the conjugate Higgs doublet,  $L_j$  is the  $SU(2)_L$  left-handed lepton doublet,  $y$  is the leptonic Yukawa coupling matrix,  $M_N$  is the Majorana mass matrix,  $C$  denotes charge conjugation, and  $R_i$  are gauge singlet right-handed neutrino fields. The number of heavy right-handed neutrinos depends on whether the lightest neutrino is massless or not [59, 60].

After spontaneous electroweak symmetry breaking, the Dirac mass matrix  $(M_D)_{ij}$  for neutrinos arises from the Yukawa interactions. The neutrino mass terms can then be expressed as

$$\frac{1}{2} \begin{bmatrix} 0 & M_D^T \\ M_D & M_N \end{bmatrix} + \text{h.c.}, \quad (2)$$

in the basis of the neutrino flavor eigenstates  $\{\nu_L, R^C\}$ . Diagonalizing this mass matrix yields three light mass eigenstates  $(\nu_i)$  and  $n$  heavy mass eigenstates  $(N_j)$ . The corresponding weak interaction terms are given by

$$\begin{aligned} \mathcal{L} \ni & -\frac{g}{\sqrt{2}}(U_{\ell i}^* \bar{\nu}_i + V_{\ell j}^* \bar{N}_j) \not{W}^+ P_L \ell + \text{h.c.} \\ & -\frac{g}{2 \cos \theta_W}(U_{\ell i}^* \bar{\nu}_i + V_{\ell j}^* \bar{N}_j) \not{Z} P_L (U_{\ell m} \nu_m + V_{\ell n} N_n), \end{aligned} \quad (3)$$

where  $g$  is the gauge coupling constant of the  $SU(2)_L$  group,  $U_{\ell i}$  ( $V_{\ell j}$ ) are the mixing parameters between the weak interaction eigenstates and the light (heavy) mass eigenstates,  $\theta_W$  is the weak-mixing angle, and  $P_L$  is the left-handed projection operator. The mixing parameters  $V_{\ell j}$  can be small [5, 8], such that the matrix  $U_{\ell i}$  is approximately unitary, *i.e.*,  $U^\dagger U \approx \mathbf{1}_{3 \times 3}$ , and can be identified with the Pontecorvo–Maki–Nakagawa–Sakata (PMNS) matrix [61–64]. Since our projected sensitivity can reach  $|V_{\ell j}| \sim 1$  in specific mass ranges, we perform a comprehensive analysis of the full  $|V_{\ell j}|$  phase space, extending up to unity.

We note that scenarios with heavy Majorana neutrinos can also provide viable explanations for the persistent  $R(D^{(*)})$  anomalies in semileptonic  $B$ -meson decays [65–67]. In particular, scenarios in which the heavy Majorana neutrino couples predominantly to the  $\tau$  flavor while its mixings with the electron and muon sectors

remain suppressed—can naturally induce the required modifications to the charged-current transition amplitudes [68, 69]. This  $\tau$ -enhanced structure is not only theoretically well-motivated but also phenomenologically attractive, as current collider constraints are significantly weaker for models dominated by  $\tau$  couplings [27, 33, 37, 70, 71].

Motivated by these considerations, we first examine a benchmark model in which the heavy Majorana neutrino couples exclusively to a single lepton flavor. We then extend our analysis to a more general framework in which  $N$  couples to all three charged-lepton generations, thereby allowing for potential lepton-universality violation.

### 3 Sample Simulations

The signal and background events are simulated and analyzed using **FeynRules** [72] with the HeavyN model files [52, 73], **MadGraph5\_aMC@NLO 3.5.6** [74, 75], and **MadWidth** [76]. The NNPDF2.3 LO parton distribution function set [77] is employed for event generation, with the proton–proton collision energy fixed at  $\sqrt{s} = 13.6$  TeV.

At the parton level, all samples are generated using identical selection requirements. Charged leptons are required to have transverse momentum  $p_T > 10$  GeV, while jets must satisfy  $p_T > 20$  GeV. The pseudorapidity of charged leptons is restricted to  $|\eta| < 2.5$ , and for jets to  $|\eta| < 5$ . The cross sections of all samples are taken directly from the **MadGraph5\_aMC@NLO** output, and calculated at LO in QCD.

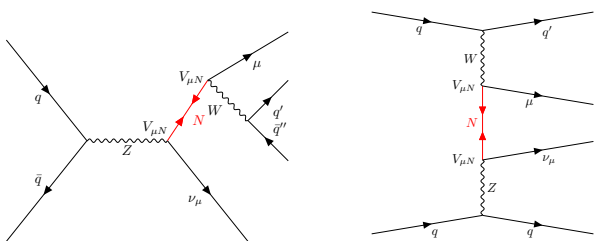


**Fig. 1** Representative Feynman diagrams illustrating the production of  $\mu\nu_{\mu}jj$  via  $s$  channel (left) and VBF processes (right), mediated by a heavy neutrino  $N$ . The parameter  $V_{\mu N}$  denotes the corresponding mixing parameter.

Signal samples are generated via pure electroweak processes  $pp \rightarrow \ell\nu jj$  at order  $\mathcal{O}(g^4)$ . Taking  $\ell = \mu$  as a representative case, we illustrate the relevant Feynman diagrams in FIG. 1 and present the signal cross section for the process  $pp \rightarrow \mu\nu_{\mu}jj$  as a function of  $m_N$  in FIG. 2. As illustrated in Fig. 2, for lower heavy neutrino masses, the heavy neutrino can be resonantly

produced through  $s$  channel processes such as Drell–Yan and  $W\gamma$  fusion [52, 53]. Compared to searches for heavy neutrinos via VBF processes leading to same-sign dilepton final states [30, 36],  $s$  channel production yields larger cross sections at low masses. However, these contributions become kinematically suppressed as  $m_N$  increases. In contrast, VBF-like topologies involving virtual heavy neutrino exchange (as shown in the right panel of Fig. 1) exhibit a milder dependence on the heavy neutrino mass. Within the inclusive  $\ell\nu jj$  final state considered in this work, these production topologies dominate in complementary mass regimes, potentially enabling sensitivity to heavy neutrinos over a broad mass range at the LHC and to smaller active–sterile mixing parameters.

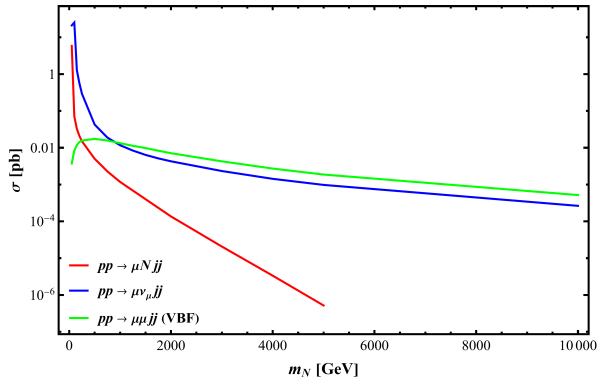


**Fig. 2** Production cross sections (with  $V_{\ell N} = 1$ ) as functions of the heavy neutrino mass  $m_N$  at a center-of-mass energy of  $\sqrt{s} = 13.6$  TeV. The red curve shows the cross section for the process  $pp \rightarrow \mu N jj$ . The blue curve corresponds to the inclusive cross section for  $pp \rightarrow \mu \nu_{\mu} jj$  while the green curve denotes the VBF-induced cross section for the same-sign dilepton channel  $pp \rightarrow \mu \mu jj$ , as used in Refs. [30, 36]. The three curves converge near  $m_N \simeq 1$  TeV, beyond which the VBF contribution becomes dominant. Our numerical results are consistent with Ref. [56].

In principle, the signal process may interfere with the SM background, for example, when the heavy neutrino is replaced by a light neutrino. However, we have evaluated the interference effects on the kinematic distributions over a wide range of heavy neutrino masses and find them to be negligible. In addition, we verify that variations in  $V_{\ell N}$  do not affect the shapes of the kinematic distributions. Together with the expected scaling of the cross section, this allows our analysis to be straightforwardly generalized to other choices of mixing parameters.

Signal samples are generated for 16 heavy neutrino mass points, ranging from 50 GeV to 10 TeV, with varying step sizes. For the SM background, we consider several sources, including single top and top-quark pair

production, single Higgs production (via gluon-gluon fusion, VBF, and associated production), vector boson production  $V = \{Z, W\}$  in association with jets, pure QCD multijet events, diboson production ( $VV = \{WW, ZZ, WZ\}$ ), and triboson processes ( $VVV$ ). Among these, the dominant backgrounds arise from  $V +$  jets and diboson production with associated jets. We therefore simulate the inclusive SM process  $pp \rightarrow \ell\nu + \geq 2j$ , including QCD contributions, which effectively captures both the  $V +$  jets and diboson components. The resulting background cross section is 1888 pb. All remaining background processes listed above are found to be subdominant and do not contribute appreciably to our analysis.

The generated parton-level events are subsequently passed to **Pythia 8.2.30** [78], where parton shower evolution and hadronization are modeled. Detector-level effects are then emulated with **Delphes 3.4.1** [79], employing CMS detector configurations for object reconstruction and particle identification. Jets are reconstructed using the anti- $k_T$  clustering scheme [80] with a radius parameter of  $R = 0.4$ , as implemented in **FastJet 3.4.2** [81]. Jet matching and merging are performed using the MLM prescription [82], with the matching scales chosen as  $XQCUT = 30$  and  $QCUT = 45$  to maintain a smooth behavior of the differential jet rates across different jet multiplicities.

Efficient reconstruction of leptons, jets initiated by light quarks or gluons, and bottom-flavored jets plays a central role in isolating signal processes from SM backgrounds and is therefore essential for maximizing sensitivity at the HL-LHC. At the same time, the large number of overlapping proton–proton interactions anticipated at the HL-LHC presents significant challenges for particle and object identification. The impact of pileup on searches for physics beyond the SM, as well as the effectiveness of pileup mitigation strategies for the CMS and ATLAS experiments, has been studied in Ref. [83]. Although a detailed evaluation of the upgraded detector performance lies beyond the scope of this analysis, we adopt conservative performance assumptions by allowing for a modest reduction in lepton and hadron identification efficiencies. These assumptions are guided by Ref. [83] and correspond to an average of 140 pileup interactions per bunch crossing.

The efficiency for reconstructing charged hadrons, which directly impacts both jet/tau reconstruction and the determination of missing transverse momentum, is taken to be approximately 97% in the pseudorapidity range  $|\eta| < 1.5$ , decreasing to about 85% at  $|\eta| = 2.5$ . For electrons and muons with transverse momentum  $p_T > 5$  GeV and  $|\eta| < 1.5$ , a baseline identification efficiency of 95% is assumed, together with a misiden-

tification probability of 0.3% [83, 84]. In the forward region,  $1.5 < |\eta| < 2.5$ , the performance is assumed to degrade linearly, reaching an identification efficiency of 65% and a misidentification rate of 0.5% at the edge of the tracker acceptance. These performance losses, primarily driven by additional proton–proton interactions, result in reduced precision in the reconstructed lepton kinematics. For bottom-quark identification, we follow Ref. [85] and employ the “Loose” working point of the DeepCSV tagger [86], which corresponds to a  $b$ -tagging efficiency of approximately 70–80% and a light-flavor mistag rate of about 10%. The specific choice of the  $b$ -tagging operating point is determined through an optimization procedure aimed at suppressing top-quark backgrounds and maximizing the overall discovery sensitivity.

A comprehensive study to address suitable and available HL-LHC triggers is beyond the scope of this work. However, we note that the CMS compressed SUSY search in [87] utilized a soft lepton plus  $E_T^{\text{miss}}$  trigger. As such, we deem it reasonable that an HL-LHC trigger be developed for the proposed search strategy in this paper.

## 4 Data Analysis

The analysis of signal and background events is performed using a machine-learning–based classifier known as gradient-boosted decision trees (BDTs) [58], which have become a standard tool in high-energy physics for multivariate classification tasks. BDTs are ensemble learning methods that combine the outputs of multiple decision trees trained sequentially to enhance predictive performance. Each tree in the sequence is trained to correct the errors made by its predecessors, with the final model constructed as a weighted sum of the individual trees. This gradient-boosting approach effectively minimizes a specified loss function in a greedy, iterative manner, allowing the model to capture complex nonlinear relationships in the input data.

One of the main strengths of BDTs lies in their ability to incorporate a large number of input features simultaneously and to automatically identify the most informative combinations. In the context of particle physics, this capability is particularly advantageous for event-classification problems, where signal and background processes may differ subtly across multiple kinematic variables. By exploiting correlations and higher-order dependencies among these variables, BDTs enable the construction of highly discriminative decision boundaries that go beyond traditional cut-based analyses. Their interpretability, flexibility, and robustness have made them a widely adopted choice in collider experiments such as those at the LHC [88–94], where distin-

guishing rare signals from overwhelming backgrounds is a central challenge.

For our analysis, we employed the BDT implementations provided by the `Scikit-learn` [95] and `XGBoost` [96] libraries. Specifically, we used the `XGBClassifier` with the objective function set to `binary: logistic`, which models the probability of a binary outcome using logistic regression. Our analysis pipeline relies on a dedicated `MadAnalysis` expert-mode C++ framework designed to process the simulated event samples and extract the relevant kinematic and event-level observables. The selected variables are reformatted and exported into a structured CSV dataset, which serves as the input for the subsequent machine-learning training. To correctly represent the relative contributions of signal and background processes, event weights derived from their respective production cross sections are applied, ensuring a statistically consistent dataset.

The weighted signal and background samples are then reprocessed within the `MadAnalysis` expert-mode environment, where an initial event selection is performed prior to CSV generation. Events are categorized into independent analysis channels according to the reconstructed lepton flavor, with each flavor treated as a separate search channel and associated with its own independently trained and validated BDT classifier. Reconstructed object-level selection requirements are imposed as follows: reconstructed electrons and muons (hadronically decaying taus) are required to satisfy  $p_T > 10$  (15) GeV and  $|\eta| < 2.5$ . To suppress backgrounds containing heavy-flavor production, events with at least one identified b-tagged jet with  $p_T > 30$  GeV and  $|\eta| < 2.5$  are vetoed. The target signal topology includes two additional hadronic jets; consequently, a dijet selection is enforced by requiring a minimum of two jets with transverse momentum  $p_T > 30$  GeV and pseudorapidity  $|\eta| < 5$ . All jet pairs satisfying these criteria are subsequently combined to construct dijet candidates.

Each model was trained with 31 kinematic features: the transverse momentum ( $p_T$ ), longitudinal momentum ( $p_z$ ), azimuthal angle ( $\phi$ ), and pseudorapidity ( $\eta$ ) of the two jets and the charged lepton; the missing transverse energy ( $E_T^{\text{miss}}$ ); the azimuthal angle of the transverse missing energy; the azimuthal angle separation ( $\Delta\phi$ ), pseudorapidity separation ( $\Delta\eta$ ), and angular separation ( $\Delta R$ ) between the two jets and between the missing transverse energy and the charged lepton; the pseudorapidity separation between the leading jet and the charged lepton; the transverse mass  $M_T$  of each visible object and missing transverse energy; visible transverse energy  $E_T$ ; hadronic transverse energy  $H_T$ ; the invariant mass ( $M$ ) of the dijet system and charged lepton; and the relative transverse momentum

between the leading jet and the charged lepton, defined as  $(p_T[j_1] - p_T[\ell])/p_T[j_1]$ . The two jets are ranked by their transverse momentum, such that  $p_T[j_1]$  and  $p_T[j_2]$  represent the leading and subleading jets, respectively.

A separate model was trained for each heavy neutrino mass, using one million signal and background events per mass point. An additional 0.5 million events were used for hyperparameter tuning via Optuna [97] with 200 trials, and a further 0.5 million events are reserved for final model validation.

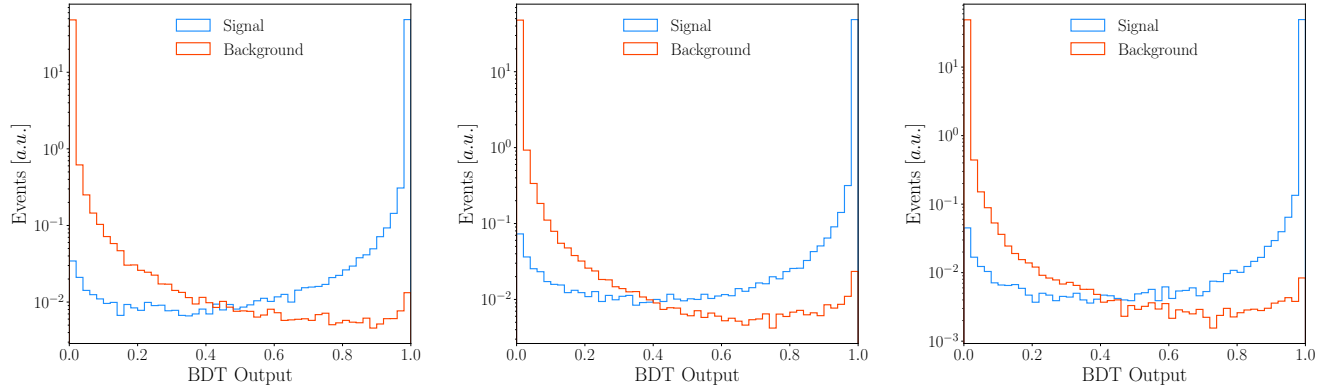
## 5 Results

FIG. 3 presents the BDT output distributions for heavy neutrino masses of 0.1, 1, and 10 TeV in the process  $pp \rightarrow \mu\nu_\mu jj$ . During BDT training, signal and background events are labeled as 1 and 0, respectively. Therefore, a score closer to 0 corresponds to background-like events, while a score closer to 1 corresponds to signal-like events.

The corresponding relative feature importance is shown in FIG. 4. The importance reflects each variable's contribution to the model's decision-making process, with kinematic features ranked according to their discriminating power between signal and background events. As shown in FIG. 4, one of the most important features is the transverse mass constructed from the missing energy and the charged lepton. For SM background processes, these two objects are most likely produced from the same  $W$  boson, resulting in a transverse mass distribution that peaks near the  $W$  boson mass. This behavior is confirmed by the corresponding event distribution shown in FIG. 5.

In VBF processes, two forward/backward jets are typically produced, while the charged lepton and missing energy are located in the central region. As a result, the dijet invariant mass  $M(j_1j_2)$  provides discrimination power. As shown in FIG. 6, for lower heavy neutrino masses, a sharp peak appears in the range  $M(j_1j_2) \sim 100$  GeV. This feature originates from resonant heavy neutrino production via the  $s$  channel, followed by its decay into an on-shell  $W$  or  $Z$  boson that subsequently decays into a dijet system. For larger heavy neutrino masses, the  $t$  channel VBF process becomes dominant, leading to a smoother  $M(j_1j_2)$  distribution with larger invariant masses typical of VBF processes [54,55,57,98–109].

At higher heavy neutrino masses, the VBF jets also exhibit larger angular separation, while the charged lepton and missing energy acquire larger transverse kinematic features such as  $p_T$ ,  $E_T$ , and  $M_T$ . These variables provide additional discrimination power against



**Fig. 3** BDT output distributions (normalized to 1) for signal and background events at heavy neutrino masses of 0.1 TeV (left), 1 TeV (middle), and 10 TeV (right) for  $\ell = \mu$ . The vertical axis shows the normalized event yield in arbitrary units, and the horizontal axis represents the BDT output score.

the background and are effectively captured by the BDT model, *e.g.*, as illustrated in FIG. 7.

For the case of  $\ell = \tau$ , we focus exclusively on hadronic  $\tau$  decays, given the reconstruction challenges associated with purely leptonic  $\tau$  decays at the LHC and the improved performance of  $\tau$ -jet identification enabled by modern machine-learning techniques [110–113]. To model this scenario—and noting that hadronic  $\tau$  decays produce several possible final states with different pion multiplicities—we use the TauDecay [114] package to simulate only the single charged-pion decay mode,  $pp \rightarrow \tau(\rightarrow \pi\nu_\tau)\nu_\tau jj$ , as a qualitative representation of hadronic  $\tau$  decays for both the signal and background, applying the same selection criteria as before. During model training, the charged lepton is replaced by a charged pion, and the missing energy includes contributions from two light neutrinos. The resulting BDT output and relative feature importance are shown in FIG. 8 and FIG. 9, respectively.

For similar reasons, the transverse mass between the charged pion and the missing energy also peaks around the  $W$  boson mass for SM backgrounds, making it one of the most important features, as confirmed by FIG. 9. However, because hadronic  $\tau$  decays involve additional neutrinos in the final state, the kinematic reconstruction is less precise, which degrades the overall discriminating power of the input variables. As a result, the BDT model efficiency in the  $\tau$  channel is reduced compared to the light lepton channels.

A shape-based, binned profile likelihood analysis of the BDT score distributions is performed using the CMS **Combine** tool [115]. Expected limits on the signal production cross sections are obtained with the asymptotic method using an Asimov dataset. All results are presented assuming an integrated luminosity of  $\mathcal{L}_{\text{int}} = 3000 \text{ fb}^{-1}$ , representative of the HL-LHC dataset. For the limit-setting procedure, the BDT output distribu-

tions (50 bins between 0–1) are scaled according to  $N = \mathcal{L}_{\text{int}} \times \sigma \times \epsilon$ , where  $\epsilon$  encapsulates event selection and reconstruction efficiencies (for the  $\tau$  channel, the hadronic  $\tau$  decay branching ratio is included in  $\epsilon$ ).

Systematic effects are incorporated directly into the likelihood through nuisance parameters. Lognormal priors are assigned to normalization-related uncertainties, while Gaussian constraints are used for uncertainties affecting the shapes of the BDT output distributions. Both experimental and theoretical sources of systematic uncertainty are considered. To account for uncertainties associated with the choice of parton distribution functions, a normalization uncertainty in the range of 1–5%, depending on the Monte Carlo sample, is applied following the PDF4LHC prescriptions [116]. This contribution has a limited impact on the total expected yields and introduces negligible distortions to the BDT output shapes when compared to the statistical fluctuations in individual bins. PDF uncertainties are treated as uncorrelated between signal and background processes, but fully correlated across the BDT bins within a given process.

Additional theoretical uncertainties arising from missing higher-order corrections in the signal cross section are evaluated by varying the renormalization and factorization scales independently by factors of two. The resulting variations in the bin-by-bin BDT yields are found to be at the level of 2–5%, depending on the heavy neutrino mass, mixing parameters, and the position within the BDT distribution.

Experimental uncertainties are implemented following current CMS performance studies. A conservative 3% uncertainty on the integrated luminosity measurement is included [117] and treated as fully correlated across all processes and BDT bins. For electrons and muons, a 2% uncertainty is assigned to reconstruction, identification, and isolation efficiencies, along with an

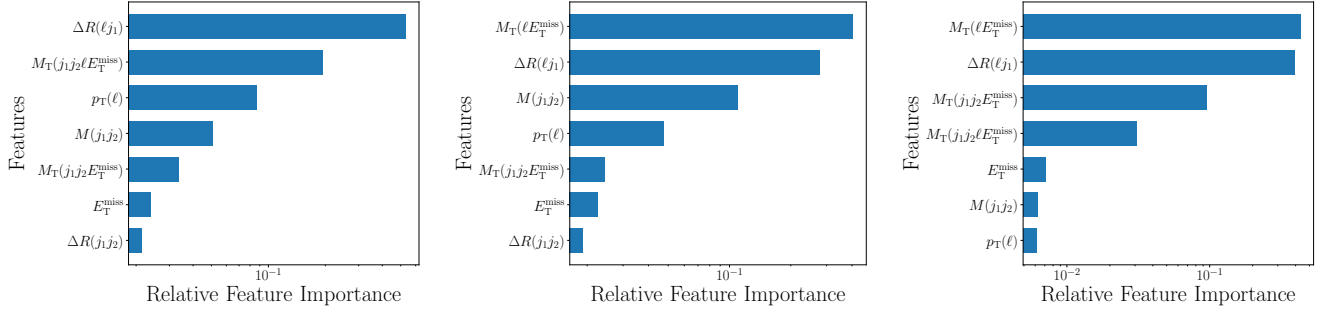


**Fig. 4** Relative feature importance for the BDT classifier at a heavy neutrino mass of 0.1 TeV (left), 1 TeV (middle), and 10 TeV (right) for  $\ell = \mu$ .

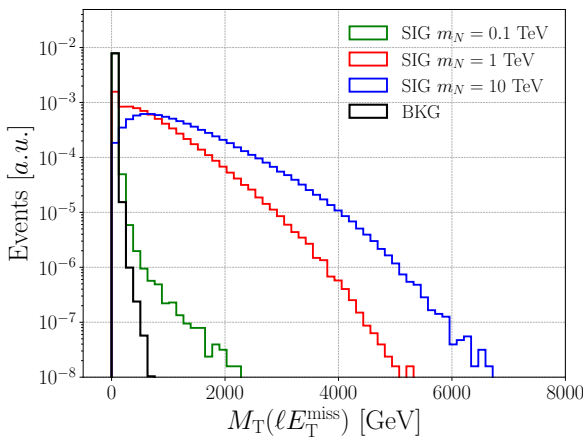


**Fig. 5** Distribution (normalized to 1) of the variable  $M_T(\ell E_T^{\text{miss}})$  for background (BKG) and signal (SIG) events corresponding to heavy neutrino masses of 0.1, 1, and 10 TeV, shown together in a single panel for  $\ell = \mu$ .

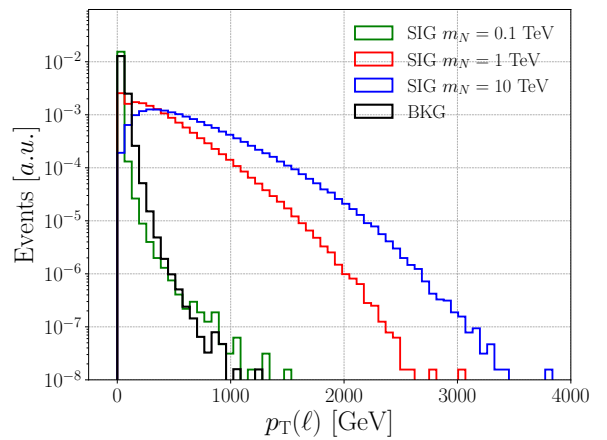


**Fig. 7** Distribution (normalized to 1) of the variable  $p_T(\ell)$  for background (BKG) and signal (SIG) events corresponding to heavy neutrino masses of 0.1, 1, and 10 TeV, shown together in a single panel for  $\ell = \mu$ .

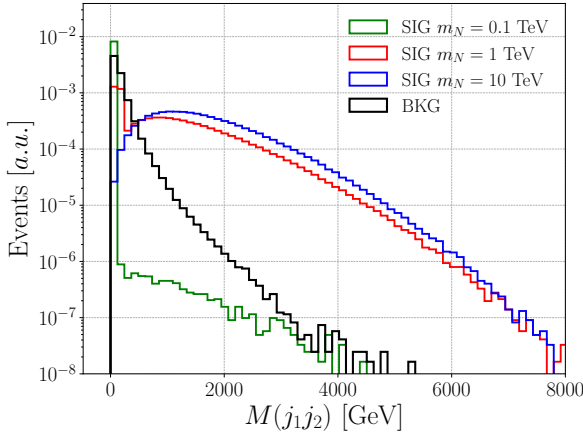


**Fig. 6** Distribution (normalized to 1) of the variable  $M(j_1 j_2)$  for background (BKG) and signal (SIG) events corresponding to heavy neutrino masses of 0.1, 1, and 10 TeV, shown together in a single panel for  $\ell = \mu$ .

additional 3% uncertainty associated with momentum and energy scale and resolution effects, assumed to be independent of lepton transverse momentum and pseudorapidity [70, 71, 118–125]. These lepton-related uncertainties are taken as correlated across all processes containing prompt leptons and across the BDT bins for each process.

Jet energy scale uncertainties, ranging between 2% and 5% depending on jet  $p_T$  and  $|\eta|$  [70, 71, 126], are propagated to the BDT output and induce shape variations of approximately 1–3% across the discriminant bins. While a data-driven calibration of SM background predictions is beyond the scope of this study, an additional normalization uncertainty of 10% is assigned to both signal and background expectations to reflect residual modeling uncertainties. This contribution is taken to be uncorrelated between signal and background processes and independent of the BDT output bin. When all systematic effects are combined, the resulting overall impact is conservatively estimated to be of order 20%.

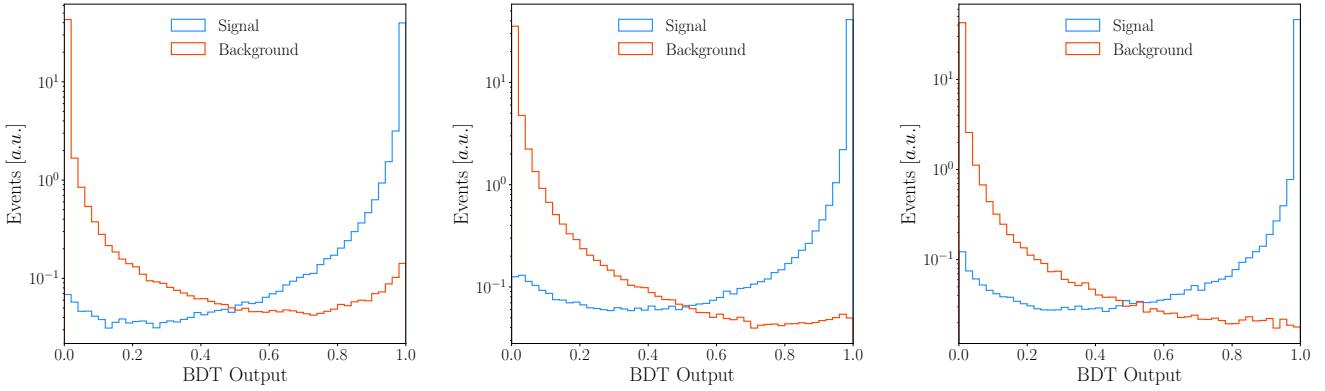


**Fig. 8** BDT output distributions (normalized to 1) for signal and background events at heavy neutrino masses of 0.1 TeV (left), 1 TeV (middle), and 10 TeV (right) for  $\ell = \tau$ . The vertical axis shows the normalized event yield in arbitrary units, and the horizontal axis represents the BDT output score.

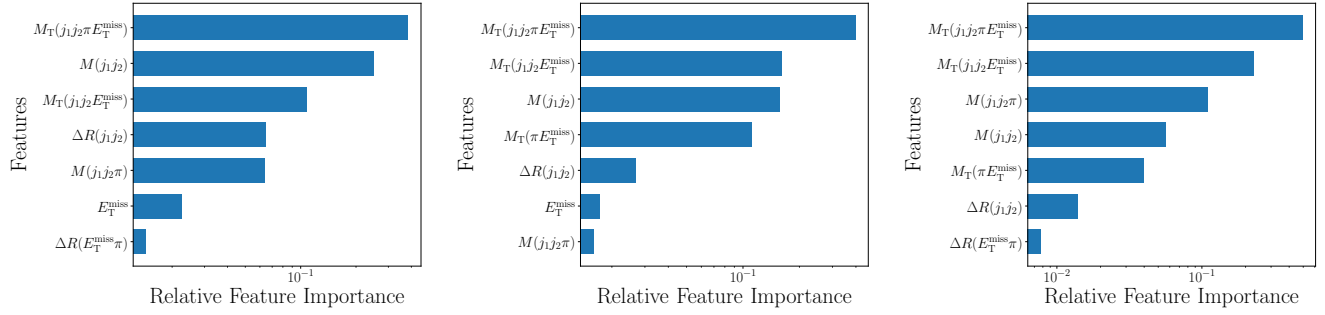


**Fig. 9** Relative feature importance for the BDT classifier at a heavy neutrino mass of 0.1 TeV (left), 1 TeV (middle), and 10 TeV (right) for  $\ell = \tau$ .

Finally, statistical uncertainties associated with the finite size of the simulated signal and background samples are included on a bin-by-bin basis in the BDT output histograms. These uncertainties range from approximately 1% to 35%, depending on the process and the specific region of the BDT discriminant, and are treated as uncorrelated across both processes and bins.

Because the relationship between the cross section and the mixing parameter varies substantially across the mass range  $m_N \in [50 \text{ GeV}, 10 \text{ TeV}]$ , we generate additional samples for different mixing parameter values within  $|V_{\ell N}|^2 \in [0, 1]$  and fit the resulting cross sections using the parameterization

$$\sigma = a|V_{\ell N}|^2 + b|V_{\ell N}|^4, \quad (4)$$

where  $a$  and  $b$  are free parameters determined independently at each mass point. This fitted relation enables us to extract the sensitivity to the mixing parameter  $|V_{\ell N}|^2$  at the HL-LHC with an integrated luminosity of  $3000 \text{ fb}^{-1}$ . The results for  $\ell = \tau$  and  $\ell = \mu$  are shown in FIG. 10 and FIG. 11, respectively.

Since the flavor of the final-state light neutrino cannot be directly identified in collider experiments, we consider combining charged-lepton and neutrino flavors

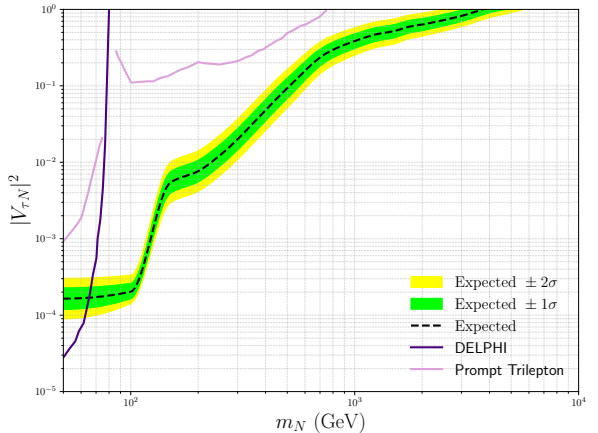


**Fig. 10** Expected upper limits at 95% confidence level on  $|V_{\tau N}|^2$  as a function of the heavy neutrino mass  $m_N$ . The solid line indicates the median expected limit, while the green and yellow bands represent the  $\pm 1\sigma$  and  $\pm 2\sigma$  expected uncertainty intervals, respectively. Results from the DELPHI [27] and prompt trilepton [33] searches are included for comparison.

to probe possible violations of lepton universality. For  $\ell = e, \mu$ , this is implemented by replacing  $|V_{\mu N}|^2$  with  $|V_{e N}|^2 + |V_{\mu N}|^2$  and combining the two channels when

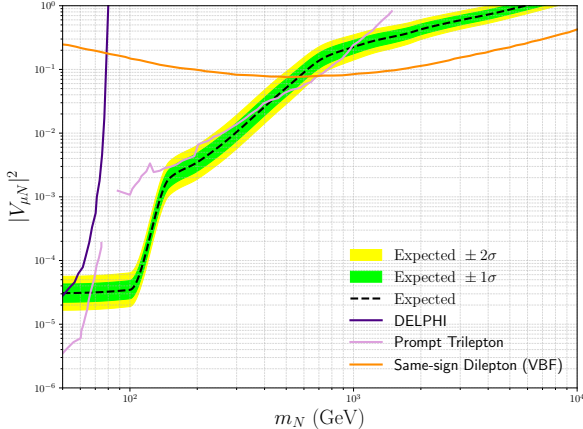


**Fig. 11** Expected upper limits at 95% confidence level on  $|V_{\mu N}|^2$  as a function of the heavy neutrino mass  $m_N$ . The solid line indicates the median expected limit, while the green and yellow bands represent the  $\pm 1\sigma$  and  $\pm 2\sigma$  expected uncertainty intervals, respectively. Results from the DELPHI [27] and prompt trilepton [33] searches are included for comparison.

computing the expected limits and uncertainties. This procedure can be straightforwardly generalized to include the  $\tau$  lepton. Since the  $\ell = e, \mu$  case is a subset of the  $\ell = e, \mu, \tau$  combination and leads to qualitatively similar results, we present only the latter in Fig. 12.

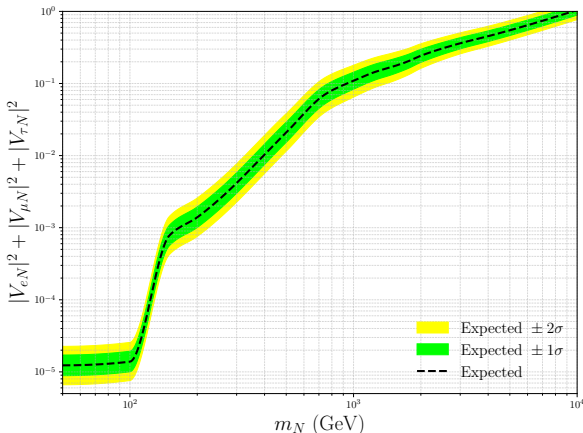


**Fig. 12** Expected upper limits at 95% confidence level on  $|V_{e N}|^2 + |V_{\mu N}|^2 + |V_{\tau N}|^2$  as a function of the heavy neutrino mass  $m_N$ . The solid line indicates the median expected limit, while the green and yellow bands represent the  $\pm 1\sigma$  and  $\pm 2\sigma$  expected uncertainty intervals, respectively.

Across FIG. 10 through FIG. 12, the sensitivity to the mixing parameter  $|V_{\ell N}|^2$  reaches values as low as  $\mathcal{O}(10^{-5})$  for a heavy neutrino mass of  $m_N = 50$  GeV, extending beyond the reach of previous searches such as those performed by DELPHI [27]. The sensitivity de-

grades rapidly as  $m_N$  increases toward the TeV scale, and then decreases more gradually as VBF production becomes dominant. Finally, unitarity of the neutrino mixing matrix restricts  $|V_{\ell N}|^2 \leq 1$ , which imposes a cutoff around  $m_N \approx 10$  TeV. In particular, we demonstrate that a novel VBF production mechanism mediated by virtual  $t$  channel heavy neutrino exchange, when combined with advanced machine-learning-based analysis techniques, can lead to a substantial enhancement in sensitivity to third-generation heavy neutrino searches involving tau leptons—an experimentally challenging regime where current constraints remain weak. For light-lepton final states, the proposed strategy can extend the discovery reach at the HL-LHC and offers a complementary probe to existing LHC search methodologies.

## 6 Conclusion

In this study, we have proposed and demonstrated a potential strategy for probing heavy neutrinos at the LHC using  $\ell\nu jj$  final states analyzed with machine-learning techniques. We simulated signal and SM background events over a broad heavy neutrino mass range from 50 GeV to 10 TeV, incorporating both  $s$  channel production—dominant at low masses—and VBF processes which become increasingly important at higher masses and maintain sensitivity in the multi-TeV regime.

By employing modern machine-learning methods, we trained BDT models on an extensive set of kinematic features, achieving strong discrimination between signal and background. The feature-importance analysis shows that transverse masses involving missing transverse energy and charged leptons provide key discriminating power. We also extended the analysis to hadronic tau decays to assess the sensitivity to the mixing parameter  $|V_{\tau N}|^2$ .

Using the CMS `Combine` tool, we obtained expected upper limits on the mixing parameter  $|V_{\ell N}|^2$  at each mass point, assuming an integrated luminosity of  $3000 \text{ fb}^{-1}$  at the HL-LHC. The projected sensitivity reaches  $\mathcal{O}(10^{-5})$  for  $m_N = 50$  GeV and remains competitive up to the multi-TeV scale. We further explored scenarios where contributions from different charged-lepton flavors are combined, enabling tests of potential lepton-universality violation and providing a more inclusive framework for heavy neutrino searches.

In conclusion, an analysis strategy that combines inclusive heavy neutrino production—encompassing both  $s$  channel and vector boson fusion mechanisms—with a machine-learning-based search significantly extends the discovery reach at hadron colliders. This approach simultaneously improves sensitivity in both the low-

and high-mass regimes and markedly improves coverage of third-generation heavy neutrinos involving  $\tau$  leptons, an experimentally challenging sector where existing constraints remain comparatively weak. This methodology complements existing search strategies and highlights promising opportunities to explore physics beyond the SM in the neutrino sector.

**Acknowledgements** We thank Umar Sohail Qureshi for discussions on the application of machine learning techniques. We gratefully acknowledge support from Vanderbilt University and the U.S. National Science Foundation. This work is supported in part by NSF Awards PHY-1945366 and PHY-2411502.

## References

- Y. Fukuda *et al.* [Super-Kamiokande], Phys. Rev. Lett. **81** (1998), 1562-1567 [arXiv:hep-ex/9807003 [hep-ex]].
- Q. R. Ahmad *et al.* [SNO], Phys. Rev. Lett. **89** (2002), 011301 [arXiv:nucl-ex/0204008 [nucl-ex]].
- F. P. An *et al.* [Daya Bay], Phys. Rev. Lett. **108** (2012), 171803 [arXiv:1203.1669 [hep-ex]].
- R. N. Mohapatra and A. Y. Smirnov, Ann. Rev. Nucl. Part. Sci. **56** (2006), 569-628 [arXiv:hep-ph/0603118 [hep-ph]].
- P. Minkowski, Phys. Lett. B **67** (1977), 421-428
- M. Gell-Mann, P. Ramond and R. Slansky, Conf. Proc. C **790927** (1979), 315-321 [arXiv:1306.4669 [hep-th]].
- T. Yanagida, Conf. Proc. C **7902131** (1979), 95-99 KEK-79-18-95.
- J. Schechter and J. W. F. Valle, Phys. Rev. D **22** (1980), 2227
- M. Magg and C. Wetterich, Phys. Lett. B **94** (1980), 61-64
- T. P. Cheng and L. F. Li, Phys. Rev. D **22** (1980), 2860
- G. Lazarides, Q. Shafi and C. Wetterich, Nucl. Phys. B **181** (1981), 287-300
- R. N. Mohapatra and G. Senjanovic, Phys. Rev. D **23** (1981), 165
- R. Foot, H. Lew, X. G. He and G. C. Joshi, Z. Phys. C **44** (1989), 441
- N. Arkani-Hamed, S. Dimopoulos, G. R. Dvali and J. March-Russell, Phys. Rev. D **65** (2001), 024032 [arXiv:hep-ph/9811448 [hep-ph]].
- M. Drewes, PoS **NUFACT2014** (2015), 001 [arXiv:1502.06891 [hep-ph]].
- K. Abe *et al.* [T2K], Phys. Rev. D **100** (2019) no.5, 052006 [arXiv:1902.07598 [hep-ex]].
- E. Cortina Gil *et al.* [NA62], Phys. Lett. B **807** (2020), 135599 [arXiv:2005.09575 [hep-ex]].
- M. Ablikim *et al.* [BESIII], Phys. Rev. D **99** (2019) no.11, 112002 [arXiv:1902.02450 [hep-ex]].
- A. V. Artamonov *et al.* [E949], Phys. Rev. D **91** (2015) no.5, 052001 [erratum: Phys. Rev. D **91** (2015) no.5, 059903] [arXiv:1411.3963 [hep-ex]].
- A. Aguilar-Arevalo *et al.* [PIENU], Phys. Rev. D **97** (2018) no.7, 072012 [arXiv:1712.03275 [hep-ex]].
- R. Aaij *et al.* [LHCb], Phys. Rev. Lett. **112** (2014) no.13, 131802 [arXiv:1401.5361 [hep-ex]].
- D. Liventsev *et al.* [Belle], Phys. Rev. D **87** (2013) no.7, 071102 [erratum: Phys. Rev. D **95** (2017) no.9, 099903] [arXiv:1301.1105 [hep-ex]].
- M. Agostini *et al.* [GERDA], Phys. Rev. Lett. **125** (2020) no.25, 252502 [arXiv:2009.06079 [nucl-ex]].
- A. Abada, V. De Romeri, S. Monteil, J. Orloff and A. M. Teixeira, JHEP **04** (2015), 051 [arXiv:1412.6322 [hep-ph]].
- A. Abada, D. Bećirević, M. Lucente and O. Sumensari, Phys. Rev. D **91** (2015) no.11, 113013 [arXiv:1503.04159 [hep-ph]].
- D. Decamp *et al.* [ALEPH], Phys. Rept. **216** (1992), 253-340
- P. Abreu *et al.* [DELPHI], Z. Phys. C **74** (1997), 57-71 [erratum: Z. Phys. C **75** (1997), 580]
- A. M. Sirunyan *et al.* [CMS], Phys. Rev. Lett. **120** (2018) no.22, 221801 [arXiv:1802.02965 [hep-ex]].
- A. M. Sirunyan *et al.* [CMS], JHEP **01** (2019), 122 [arXiv:1806.10905 [hep-ex]].
- A. Tumasyan *et al.* [CMS], Phys. Rev. Lett. **131** (2023) no.1, 011803 [arXiv:2206.08956 [hep-ex]].
- A. Tumasyan *et al.* [CMS], JHEP **07** (2022), 081 [arXiv:2201.05578 [hep-ex]].
- A. Hayrapetyan *et al.* [CMS], JHEP **03** (2024), 105 [arXiv:2312.07484 [hep-ex]].
- A. Hayrapetyan *et al.* [CMS], JHEP **06** (2024), 123 [arXiv:2403.00100 [hep-ex]].
- G. Aad *et al.* [ATLAS], JHEP **10** (2019), 265 [arXiv:1905.09787 [hep-ex]].
- G. Aad *et al.* [ATLAS], Eur. Phys. J. C **83** (2023) no.9, 824 [arXiv:2305.14931 [hep-ex]].
- G. Aad *et al.* [ATLAS], Phys. Lett. B **856** (2024), 138865 [arXiv:2403.15016 [hep-ex]].
- G. Aad *et al.* [ATLAS], Phys. Rev. D **110** (2024) no.11, 112004 [arXiv:2408.05000 [hep-ex]].
- A. Hayrapetyan *et al.* [CMS], JHEP **02** (2025), 036 [arXiv:2407.10717 [hep-ex]].
- A. Hayrapetyan *et al.* [CMS], Phys. Rev. D **110** (2024), 012004 [arXiv:2402.18658 [hep-ex]].
- G. Aad *et al.* [ATLAS], JHEP **07** (2025), 196 [arXiv:2503.16213 [hep-ex]].
- S. Antusch and O. Fischer, JHEP **05** (2015), 053 [arXiv:1502.05915 [hep-ph]].
- S. Antusch, E. Cazzato and O. Fischer, Int. J. Mod. Phys. A **32** (2017) no.14, 1750078 [arXiv:1612.02728 [hep-ph]].
- S. Antusch, E. Cazzato and O. Fischer, JHEP **12** (2016), 007 [arXiv:1604.02420 [hep-ph]].
- W. Liao and X. H. Wu, Phys. Rev. D **97** (2018) no.5, 055005 [arXiv:1710.09266 [hep-ph]].
- Z. S. Wang and K. Wang, Phys. Rev. D **101** (2020) no.7, 075046 [arXiv:1911.06576 [hep-ph]].
- J. N. Ding, Q. Qin and F. S. Yu, Eur. Phys. J. C **79** (2019) no.9, 766 [arXiv:1903.02570 [hep-ph]].
- Y. Gao and K. Wang, Phys. Rev. D **105** (2022) no.7, 076005 [arXiv:2102.12826 [hep-ph]].
- A. Blondel and P. Janot, Eur. Phys. J. Plus **137** (2022) no.1, 92 [arXiv:2106.13885 [hep-ex]].
- S. Knapen and A. Thamm, Eur. Phys. J. Plus **136** (2021) no.9, 936 [arXiv:2108.08949 [hep-ph]].
- Y. F. Shen, J. N. Ding and Q. Qin, Eur. Phys. J. C **82** (2022) no.5, 398 [arXiv:2201.05831 [hep-ph]].
- L. Bellagamba, G. Polesello and N. Valle, Eur. Phys. J. C **85** (2025) no.9, 1069 [arXiv:2503.19464 [hep-ex]].
- D. Alva, T. Han and R. Ruiz, JHEP **02** (2015), 072 [arXiv:1411.7305 [hep-ph]].
- A. Flórez, K. Gui, A. Gurrola, C. Patiño and D. Restrepo, Phys. Lett. B **778** (2018), 94-100 [arXiv:1708.03007 [hep-ph]].

54. A. G. Delannoy, B. Dutta, A. Gurrola, W. Johns, T. Kamon, E. Luiggi, A. Melo, P. Sheldon, K. Sinha and K. Wang, *et al.* Phys. Rev. Lett. **111** (2013), 061801 [arXiv:1304.7779 [hep-ph]].

55. V. Khachatryan *et al.* [CMS], Phys. Rev. Lett. **118** (2017) no.2, 021802 [arXiv:1605.09305 [hep-ex]].

56. B. Fuks, J. Neundorf, K. Peters, R. Ruiz and M. Saimpert, Phys. Rev. D **103** (2021) no.5, 055005 [arXiv:2011.02547 [hep-ph]].

57. A. Hayrapetyan *et al.* [CMS], Phys. Rev. Lett. **135** (2025) no.6, 061803 [arXiv:2412.19261 [hep-ex]].

58. J. H. Friedman, Annals Statist. **29** (2001) no.5, 1189-1232

59. D. Wyler and L. Wolfenstein, Nucl. Phys. B **218** (1983), 205-214

60. S. F. King, J. Phys. G **42** (2015), 123001 [arXiv:1510.02091 [hep-ph]].

61. B. Pontecorvo, Sov. Phys. JETP **7** (1958), 172-173

62. Z. Maki, M. Nakagawa and S. Sakata, Prog. Theor. Phys. **28** (1962), 870-880

63. B. Pontecorvo, Sov. Phys. JETP **26** (1968), 984-988

64. S. Navas *et al.* [Particle Data Group], Phys. Rev. D **110** (2024) no.3, 030001

65. J. P. Lees *et al.* [BaBar], Phys. Rev. Lett. **109** (2012), 101802 [arXiv:1205.5442 [hep-ex]].

66. J. P. Lees *et al.* [BaBar], Phys. Rev. D **88** (2013) no.7, 072012 [arXiv:1303.0571 [hep-ex]].

67. R. Aaij *et al.* [LHCb], Phys. Rev. Lett. **115** (2015) no.11, 111803 [erratum: Phys. Rev. Lett. **115** (2015) no.15, 159901] [arXiv:1506.08614 [hep-ex]].

68. A. Atre, T. Han, S. Pascoli and B. Zhang, JHEP **05** (2009), 030 [arXiv:0901.3589 [hep-ph]].

69. L. Calibbi, A. Crivellin and T. Ota, Phys. Rev. Lett. **115** (2015), 181801 [arXiv:1506.02661 [hep-ph]].

70. V. Khachatryan *et al.* [CMS], JHEP **03** (2017), 077 [arXiv:1612.01190 [hep-ex]].

71. A. M. Sirunyan *et al.* [CMS], JHEP **03** (2019), 170 [arXiv:1811.00806 [hep-ex]].

72. A. Alloul, N. D. Christensen, C. Degrande, C. Duhr and B. Fuks, Comput. Phys. Commun. **185** (2014), 2250-2300 [arXiv:1310.1921 [hep-ph]].

73. C. Degrande, O. Mattelaer, R. Ruiz and J. Turner, Phys. Rev. D **94** (2016) no.5, 053002 [arXiv:1602.06957 [hep-ph]].

74. J. Alwall, R. Frederix, S. Frixione, V. Hirschi, F. Maltoni, O. Mattelaer, H. S. Shao, T. Stelzer, P. Torrielli and M. Zaro, JHEP **07** (2014), 079 [arXiv:1405.0301 [hep-ph]].

75. R. Frederix, S. Frixione, V. Hirschi, D. Pagani, H. S. Shao and M. Zaro, JHEP **07** (2018), 185 [erratum: JHEP **11** (2021), 085] [arXiv:1804.10017 [hep-ph]].

76. J. Alwall, C. Duhr, B. Fuks, O. Mattelaer, D. G. Öztürk and C. H. Shen, Comput. Phys. Commun. **197** (2015), 312-323 [arXiv:1402.1178 [hep-ph]].

77. R. D. Ball, V. Bertone, S. Carrazza, C. S. Deans, L. Del Debbio, S. Forte, A. Guffanti, N. P. Hartland, J. I. Latorre and J. Rojo, *et al.* Nucl. Phys. B **867** (2013), 244-289 [arXiv:1207.1303 [hep-ph]].

78. T. Sjöstrand, S. Ask, J. R. Christiansen, R. Corke, N. Desai, P. Ilten, S. Mrenna, S. Prestel, C. O. Rasmussen and P. Z. Skands, Comput. Phys. Commun. **191** (2015), 159-177 [arXiv:1410.3012 [hep-ph]].

79. J. de Favereau *et al.* [DELPHES 3], JHEP **02** (2014), 057 [arXiv:1307.6346 [hep-ex]].

80. M. Cacciari, G. P. Salam and G. Soyez, JHEP **04** (2008), 063 [arXiv:0802.1189 [hep-ph]].

81. M. Cacciari, G. P. Salam and G. Soyez, Eur. Phys. J. C **72** (2012), 1896 [arXiv:1111.6097 [hep-ph]].

82. M. L. Mangano, M. Moretti, F. Piccinini and M. Trecanani, JHEP **01** (2007), 013 [arXiv:hep-ph/0611129 [hep-ph]].

83. [CMS], at CMS with 3000/fb,” CMS-PAS-FTR-13-014.

84. A. M. Sirunyan *et al.* [CMS], JINST **15** (2020) no.02, P02027 [arXiv:1912.03516 [physics.ins-det]].

85. A. M. Sirunyan *et al.* [CMS], JINST **13** (2018) no.05, P05011 [arXiv:1712.07158 [physics.ins-det]].

86. E. Bols, J. Kieseler, M. Verzetti, M. Stoye and A. Stakia, JINST **15** (2020) no.12, P12012 [arXiv:2008.10519 [hep-ex]].

87. A. M. Sirunyan *et al.* [CMS], Phys. Lett. B **782** (2018), 440-467 [arXiv:1801.01846 [hep-ex]].

88. B. P. Roe, H. J. Yang, J. Zhu, Y. Liu, I. Stancu and G. McGregor, Nucl. Instrum. Meth. A **543** (2005) no.2-3, 577-584 [arXiv:physics/0408124 [physics]].

89. S. Chatrchyan *et al.* [CMS], Phys. Rev. D **89** (2014) no.1, 012003 [arXiv:1310.3687 [hep-ex]].

90. P. Baldi, P. Sadowski and D. Whiteson, Nature Commun. **5** (2014), 4308 [arXiv:1402.4735 [hep-ph]].

91. M. Aaboud *et al.* [ATLAS], Phys. Rev. D **97** (2018) no.7, 072016 [arXiv:1712.08895 [hep-ex]].

92. K. Albertsson, P. Altoe, D. Anderson, J. Anderson, M. Andrews, J. P. Araque Espinosa, A. Aurisano, L. Basara, A. Bevan and W. Bhimji, *et al.* J. Phys. Conf. Ser. **1085** (2018) no.2, 022008 [arXiv:1807.02876 [physics.comp-ph]].

93. D. Barbosa, F. Díaz, L. Quintero, A. Flórez, M. Sanchez, A. Gurrola, E. Sheridan and F. Romeo, Eur. Phys. J. C **83** (2023) no.5, 413 [arXiv:2210.15813 [hep-ph]].

94. U. S. Qureshi, A. Gurrola, A. Flórez and C. Rodriguez, Eur. Phys. J. C **85** (2025) no.4, 379 [arXiv:2410.17854 [hep-ph]].

95. F. Pedregosa, G. Varoquaux, A. Gramfort, O. Grisel, M. Blondel, A. Müller, J. Nothman, G. Louppe, P. Prettenhofer and R. Weiss, *et al.* J. Machine Learning Res. **12** (2011), 2825-2830 [arXiv:1201.0490 [cs.LG]].

96. T. Chen and C. Guestrin, [arXiv:1603.02754 [cs.LG]].

97. T. Akiba, S. Sano, T. Yanase, T. Ohta and M. Koyama, [arXiv:1907.10902 [cs.LG]].

98. U. S. Qureshi, A. Gurrola and A. Flórez, Eur. Phys. J. C **85** (2025) no.10, 1208 [arXiv:2411.13837 [hep-ph]].

99. N. Cardona, F. Andrés, G. Alfredo, J. Will, S. Paul and T. cheng, JHEP **11** (2022), 026 [arXiv:2102.10194 [hep-ph]].

100. A. Flórez, A. Gurrola, W. Johns, P. Sheldon, E. Sheridan, K. Sinha and B. Soubasis, Phys. Rev. D **103** (2021) no.9, 095001 [arXiv:2101.11119 [hep-ph]].

101. A. M. Sirunyan *et al.* [CMS], JHEP **08** (2019), 150 [arXiv:1905.13059 [hep-ex]].

102. A. Flórez, A. Gurrola, W. Johns, J. Maruri, P. Sheldon, K. Sinha and S. R. Starko, Phys. Rev. D **100** (2019) no.1, 016017 [arXiv:1902.01488 [hep-ph]].

103. A. Flórez, Y. Guo, A. Gurrola, W. Johns, O. Ray, P. Sheldon and S. Starko, Phys. Rev. D **99** (2019) no.3, 035034 [arXiv:1812.06824 [hep-ph]].

104. A. Flórez, A. Gurrola, W. Johns, Y. D. Oh, P. Sheldon, D. Teague and T. Weiler, Phys. Lett. B **767** (2017), 126-132 [arXiv:1609.09765 [hep-ph]].

105. V. Khachatryan *et al.* [CMS], JHEP **11** (2015), 189 [arXiv:1508.07628 [hep-ex]].

106. B. Dutta, A. Gurrola, K. Hatakeyama, W. Johns, T. Kamon, P. Sheldon, K. Sinha, S. Wu and Z. Wu, Phys. Rev. D **92** (2015) no.9, 095009 [arXiv:1507.01001 [hep-ph]].

---

107. B. Dutta, T. Ghosh, A. Gurrola, W. Johns, T. Kamon, P. Sheldon, K. Sinha, K. Wang and S. Wu, Phys. Rev. D **91** (2015) no.5, 055025 [arXiv:1411.6043 [hep-ph]].

108. B. Dutta, W. Flanagan, A. Gurrola, W. Johns, T. Kamon, P. Sheldon, K. Sinha, K. Wang and S. Wu, Phys. Rev. D **90** (2014) no.9, 095022 [arXiv:1312.1348 [hep-ph]].

109. B. Dutta, A. Gurrola, W. Johns, T. Kamon, P. Sheldon and K. Sinha, Phys. Rev. D **87** (2013) no.3, 035029 [arXiv:1210.0964 [hep-ph]].

110. A. M. Sirunyan *et al.* [CMS], JINST **13** (2018) no.10, P10005 [arXiv:1809.02816 [hep-ex]].

111. A. Tumasyan *et al.* [CMS], JINST **17** (2022), P07023 [arXiv:2201.08458 [hep-ex]].

112. [ATLAS], ATL-PHYS-PUB-2022-044.

113. A. Hayrapetyan *et al.* [CMS], JINST **20** (2025) no.12, P12032 [arXiv:2511.05468 [hep-ex]].

114. K. Hagiwara, T. Li, K. Mawatari and J. Nakamura, Eur. Phys. J. C **73** (2013), 2489 [arXiv:1212.6247 [hep-ph]].

115. A. Hayrapetyan *et al.* [CMS], Comput. Softw. Big Sci. **8** (2024) no.1, 19 [arXiv:2404.06614 [physics.data-an]].

116. J. Butterworth, S. Carrazza, A. Cooper-Sarkar, A. De Roeck, J. Feltesse, S. Forte, J. Gao, S. Glazov, J. Huston and Z. Kassabov, *et al.* J. Phys. G **43** (2016), 023001 [arXiv:1510.03865 [hep-ph]].

117. E. Ayala *et al.* [CMS BRIL], Eur. Phys. J. C **83** (2023) no.7, 673 [arXiv:2206.08870 [physics.ins-det]].

118. A. M. Sirunyan *et al.* [CMS], JHEP **07** (2017), 121 [arXiv:1703.03995 [hep-ex]].

119. A. Hayrapetyan *et al.* [CMS], Phys. Rev. D **111** (2025) no.11, 112004 [arXiv:2412.04357 [hep-ex]].

120. C. Avila, A. Flórez, A. Gurrola, D. Julson and S. Starko, Phys. Dark Univ. **27** (2020), 100430 [arXiv:1801.03966 [hep-ph]].

121. V. Khachatryan *et al.* [CMS], JHEP **02** (2017), 048 [arXiv:1611.06594 [hep-ex]].

122. A. Flórez, L. Bravo, A. Gurrola, C. Ávila, M. Segura, P. Sheldon and W. Johns, Phys. Rev. D **94** (2016) no.7, 073007 [arXiv:1606.08878 [hep-ph]].

123. S. Chatrchyan *et al.* [CMS], Eur. Phys. J. C **73** (2013), 2493 [arXiv:1301.3792 [hep-ex]].

124. S. Chatrchyan *et al.* [CMS], Phys. Lett. B **716** (2012), 82-102 [arXiv:1206.1725 [hep-ex]].

125. A. Flórez, J. Jones-Pérez, A. Gurrola, C. Rodriguez and J. Peñuela-Parra, Eur. Phys. J. C **83** (2023) no.11, 1023 [arXiv:2307.11070 [hep-ph]].

126. A. M. Sirunyan *et al.* [CMS], Phys. Lett. B **819** (2021), 136446 [arXiv:2012.04178 [hep-ex]].